



Synchrotron Radiography for a Proton Exchange Membrane (PEM) Electrolyzer[▲]

U. Panchenko¹, T. Arlt², I. Manke³, M. Müller^{1*}, D. Stolten^{1,4}, W. Lehnert^{1,5}

¹ Institute of Energy and Climate Research, Electrochemical Process Engineering (IEK-3), Forschungszentrum Jülich GmbH, Jülich, Germany

² Technische Universität Berlin, Institute for Materials Science, Berlin, Germany

³ Institute of Applied Materials, Helmholtz-Zentrum Berlin, Berlin, Germany

⁴ Chair for Fuel Cells, RWTH Aachen University, Aachen, Germany

⁵ Faculty of Mechanical Engineering, RWTH Aachen University, Aachen, Germany

Received June 11, 2019; accepted January 08, 2020; published online February 17, 2020

Abstract

In-plane synchrotron radiography with a resolution of a few micrometers was applied to study transport processes within a Proton Exchange Membrane (PEM) electrolyzer cell. The degradation process of the catalyst layer, gas production with bubble formation at the catalyst layer and in the porous transport layer (PTL) was analyzed. From this, a new cell design was developed that allows for high X-ray transmittances at the membrane plane in the in-plane viewing direction. During the measurement, a bubble growth and move-

ment was observed. Furthermore, a detachment of catalytic material from the catalyst layer was detected. Afterwards, a *post mortem* EDX analysis was conducted to determine the position of the catalyst particles. Despite Iridium being initially used as the anode catalyst and platinum as the cathode catalyst, the EDX measurement revealed Pt and Ir particles on both electrodes following cell operation.

Keywords: Blistering in Porous Materials, Catalyst Layer Degradation, PEM Electrolysis, Synchrotron Radiography, Two-phase Flow

1 Introduction

Electrolysis is an important component in the transition of the energy system towards a renewable basis. One application of electrolysis is the power-to-gas concept, in which chemically-bound energy is released as electrical energy. Energy production with solar installations and wind turbines is highly dependent on the weather, which can be compensated by storing excess energy in the form of hydrogen.

In an electrolysis cell, water is added and gas is produced: oxygen on the anode side and hydrogen on the cathode side. It is a two-phase flow with gaseous hydrogen, water vapor and liquid water. System characterization and description is further complicated because this two-phase flow occurs in a porous material, namely a porous transport layer (PTL). The PTL is essential for homogeneous water distribution and efficient gas discharge. Such layers are frequently porous structures sintered from titanium powder or made of titanium mesh.

Gas produced in the form of bubbles can partially cover the catalyst and impede the access of the water to the catalyst and

thus hinder the electrochemical reaction. Such gas accumulations, also called mass transport limitations, can cause overpotentials which have to be avoided. The aim is to better understand multi-phase transport in the titanium based PTL and thus ensure efficient gas discharge. The investigation of the bubble formation becomes difficult, as it takes place in the small pores of a porous medium and a high local resolution is necessary. The solution to this is the use of synchrotron radiography, which allows for very good contrast between water and gas in the pores of the PTL. Mass transport limitations and overpotentials have been investigated by Roy et al. [1].

Selamet et al. [2] use soft X-ray radiography to visualize the behavior of gas bubbles. The in-plane measurement shows how the gas bubbles first develop in the PTL in different operating modes, then grow to the PTL surface and are finally discharged. Leonard et al. [3] use X-ray computed tomography (CT) and radiography in parallel to study morphology,

[*] Corresponding author, mar.mueller@fz-juelich.de

 This is an open access article under the terms of the Creative Commons Attribution-NonCommercial-NoDerivs License, which permits use and distribution in any medium, provided the original work is properly cited, the use is non-commercial and no modifications or adaptations are made.

[▲] Paper presented at the 8th International Conference on Fundamentals and Development of Fuel Cells (FDFC2019), held 12–14.02.2019 in Nantes, France.

oxygen bubble formation and bubble removal under PEM electrolyzer operating conditions. In other studies, synchrotron radiography was used and blistering between the land and channel of an electrolysis cell was observed [4, 5]. Bubble size and the growth cycle were also investigated depending on the operating points. Markötter et al. [6] combined synchrotron radiography and synchrotron tomography to investigate the water distribution in the PTL of a fuel cell. In case of fuel cells the porous transport layers are usually made of graphite fibers. Monochromatic synchrotron radiation is also well-suited to analyses of the degradation processes of catalyst layers [7, 8]. These effects can also be analyzed on a smaller scale by combining synchrotron radiography and focused ion beam tomography [9]. Hinebaugh and Lee et al. [10, 11] used synchrotron radiation to investigate water percolation in the porous layers of a fuel cell. Droplet formation and propagation were visualized.

According to conventional concepts, the gas bubble forms directly at the catalyst. Lubetkin et al. [12] showed that when the gas concentration in a water solution exceeds a critical limit, gas bubbles form in the liquid or on the PTL surface. Interfacial strain, the contact angle and oversaturation determine whether the bubbles form on the catalyst surface or in the PTL pores. In order to maintain water electrolysis, water must first diffuse to the catalyst surface. The reaction on the catalyst surface can then proceed faster than the transport of the reactants. A study by Chen et al. [13] showed that the time of bubble formation does not depend on the operating point (e.g., current density), but rather on the concentration of the gas dissolved in the water at the surface of a catalyst. The surface roughness also influences the process of gas bubble growth and detachment. Catalysts with a higher surface roughness lead to faster bubble detachment and thus reduce the bubble size [14]. Some studies [15, 16] have shown that bubble formation improves mass transport. Bubbles in the channel increase PTL through-flow. Lee et al. [17] observed a change in gas distribution in the PTL from the catalyst-coated membrane (CCM) to the channel. At the CCM, fairly smaller bubbles are present. In the direction of the canal, individual transport paths grow together and larger bubbles are observed.

Next, we wanted to investigate catalyst degradation, as the in-plane measurement allows visualization of catalyst separation and movement in the PTL pores.

The cathode catalyst is usually made of carbon-supported platinum particles. The aging and degradation processes discussed in literature point to the reduction of the available electrochemically active platinum surface (ECSA). The platinum particles migrate and reducing the ECSA. The consequence of this platinum migration is local de-passivation of the surface caused by place exchange processes in the catalyst layer. In case of fuel cells this is caused by oxide formation and oxide reduction along with molecular oxygen evolution in addition to the Platinum dissolution [18]. In PEM electrolysis additional degradation processes occur, the increase of contact resistance and the associated loss of performance is described in [19] and

on the other hand particle agglomeration known as Ostwald ripening, causes agglomerates to grow larger, as small agglomerates get smaller and disappears [20]. Catalyst particles are usually sintering together to agglomerates of a number of catalyst particles, reducing the surface area to volume ratio of the particles in each case. This mainly occurs at the high potential at the cathode of a PEM fuel cell. In the cathode of the PEM electrolyzer, the potentials are much lower and degradation would be expected to be much less severe. But particles detach from the carrier and lose electrical contact with the electrode, in which case the catalyst particle is no longer available for catalysis.

LaConti et al. [21] provide an overview of studies on membrane degradation in fuel cells in the last 30 years and compare it with electrolysis. The authors distinguish between chemical and mechanical influences on membrane degradation. Mechanical stress factors include thermal membrane expansion, as well as membrane damage from the PTL surface. Chemical stress is caused by the formation of peroxy radicals, which attack the membrane. A higher temperature accelerates the chemical degradation processes.

Grigoriev et al. [22] describe a degradation mechanism in the electrolysis cell in which the platinum diffuses through the membrane. This aging phenomenon is known in the PEM literature as platinum ribbon. Debe et al. [23] demonstrated the platinum particles used as the cathode catalyst on the anode side after 1,500 h of operation. Iridium diffuses from the anode to the cathode side, with the anode catalyst layer showing a crystallite enlargement of 40%. As a conclusion of the elemental analysis, two migration processes were suspected. The anode catalyst (Ir) diffuses to the cathode side and the cathode catalyst (Pt) to the anode side. There is a catalyst migration in each opposing direction. However, the element detection in the membrane (platinum ribbon) was not carried out. Feng et al. summarize the degradation phenomena of PEM electrolysis and offer an idea of what future research trends could be [24].

As we have already performed tests with neutron radiography at the beamline at Helmholtz Center Berlin [25] we have found that the spatial resolution of this device is limited to around 6.3 μm . We also now about the higher resolution of other neutron sources, for an example up to 1.5 μm at the NIST [26] but due to the limited availability in this study, synchrotron X-ray radiographic imaging was employed to dynamically visualize the bubble formation and catalyst degradation. With a combination of synchrotron radiography and in-plane measurement, it is possible to study not only bubble formation as a function of operating conditions, but also the propagation of bubbles in the pores of a PTL. We aim to verify the theory of Lubetkin et al. [12] as to whether bubbles form not only on the catalyst surface, but also on the PTL surface, when the super saturation of gas in water has been achieved. We also want to visualize the change in catalyst layer *operando*. Subsequently, the distribution of chemical elements in PTL is investigated *post mortem*.

2 Experimental

To experimentally investigate the gas-water transport *operando*, an electrolysis cell suitable for synchrotron radiography was designed (Figure 1). In-plane measurement was then used to investigate gas production and transport inside the PTL and the degradation processes at the boundary between the CCM and PTL. Due to the limited penetration depth of the synchrotron beam and strong absorption by the titanium material, as little material as possible should be located in the beam direction (see Figure 1a gives the view from the side and 1b gives the front view). This challenge was resolved by contacting the CCM on both sides, not with the surfaces of two sintered bodies, but rather with their lateral edges. Water was supplied to both the anode and cathode, so that one could observe the two-phase flow on both sides (cathode and anode).

The electrolysis cell was assembled with a PTL sample made from shapeless, sintered titanium particles fabricated using the hydride-dehydride (HDH) process, with a particle fraction below 45 μm. The sample thickness was 1,200 μm and its porosity was 45%. Pore size distribution was measured by mercury porosimetry. Pore radius is logarithmic normal distributed with the peak at 6 μm and a full width at half maximum (FWHM) of 4 μm. Only 0.5% of all pores are larger than 10 μm. But if you look at pore volumes, 0.5% pores make up 99.6% of all pore volumes. As an example, there are only 0.0006% of pores around 100 μm in size, but they form almost 40% pore volume. Each sintered body part had dimensions of 10 × 4.5 × 1.2 mm³, with an active surface of 10 × 1.2 mm².

In the experiment, we used home-made CCMs that were made using the decal process. A Nafion membrane coated with a catalyst was also used. This was the Nafion N117 membrane from DuPont, with an iridium loading of 2.2 mg cm⁻², and a platinum loading of 0.8 mg cm⁻².

Each end plate of the cell had two water connections on opposite sides, a depression for the PTL and CCM, two distribution channels to homogeneously distribute the water and holes to bolt the cell together with a torque of 5 Nm. Two sintered bodies also contacted the CCM with their lateral edge. The CCM was inserted between two sintered bodies in an “S”-like shape. Metal pins were then used to guarantee electrical contact. Such metal contact pins have threads and are screwed into the cell. While inserting the contact pins, the PTL plates

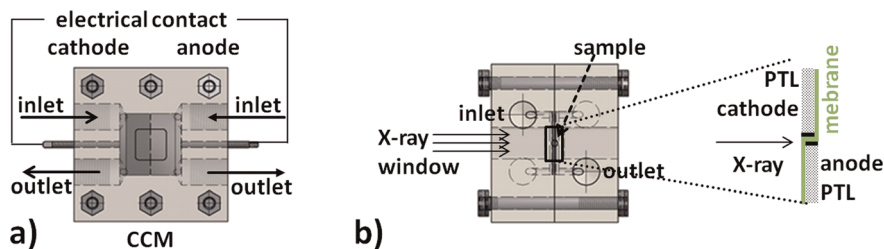


Fig. 1 Schematic cell construction: a) view of the cell from the beam direction; b) lateral view of the cell; c) two PTL are contacted with the edge to a CCM, with the synchrotron beam, the central area is visualized.

were also pressed together. Contact pins were used by hand, and it cannot be said what force the PTL and CCM printed together. In order to minimize the thickness of the acrylic glass (Plexiglas) in the beam path, depressions of 5 × 5 mm² were also milled into both end plates. The Plexiglas end plate thickness was 2.5 mm in the beam direction. As the cell end plates were made of Plexiglas, there was no possibility of heating the cell. Therefore, the cells were operated at room temperature.

The radiographic measurements were performed at BAM-line at the Helmholtz Center in Berlin, Germany [27]. According to the specifications of the camera used during the synchrotron measurement, structures in the range of about 0.5 μm can be resolved within a field of view of 1.7 × 1.2 mm² (4,008 × 2,672 pixels). The specified resolution is checked with a Siemens Star device so that we are sure the structures of a few μm in size can indeed be distinguished. The camera model was a pco4000 combined with a 20 μm Gadox scintillator. The temporal resolution was 2 s. During the measurement, the beam energy was adjusted to 16 keV and Al 0.5 mm and Be 0.5 mm metal filters were used to form the synchrotron beam.

The synchrotron beam loses intensity when passing the cell, as intensity is absorbed by the cell components. The part of the beam that is not absorbed is detected as the transmitted intensity. The Lambert-Beer law outlines how the beam intensity is attenuated during transmission through the material. The attenuation depends exponentially on the material attenuation coefficient and the material thickness:

$$I_t = I_0 \cdot e^{-\sum \mu \cdot z} \quad (1)$$

where I_0 is the original beam intensity, I_t is the transmitted intensity, μ is the mass attenuation coefficient and z is the material thickness.

In practice, an image or image series with a defined state of the cell is required, e.g., a completely wet or dry cell. For the following analyses, all other images are divided by this normalization (completely wet) image.

$$I_w = I_0 \cdot e^{-(\mu_w z_w + \mu_p z_p)} \quad (2)$$

$$I_d = I_0 \cdot e^{-(\mu_w z_d + \mu_p z_p)} \quad (3)$$

where I_w is the beam intensity of a completely wet state, I_d is the beam intensity of the other “dry” state, μ_w is the mass attenuation coefficient of water and z_w is the water thickness, while μ_p is the mass attenuation coefficient of Plexiglas and z_p the plexiglas thickness.

If we divide Eq. (2) by Eq. (3), many unknown parameters will be truncated.

$$I_w/I_d = e^{-\mu_w(z_w - z_d)} \quad (4)$$

$$(z_w - z_d) = -\frac{1}{\mu} \ln(I_w/I_d) \quad (5)$$

$(z_w - z_d)$ presents the gas fraction that has displaced the water. Further image processing follows in accordance with the Lambert-Beer law; the images produced by normalization of the logarithm of the radiation's intensity relation was taken for all images. Subsequently, these images were divided by the attenuation coefficient of water, which is about $\mu = 0.11 \text{ mm}^{-1}$ for $E = 16 \text{ keV}$. The result describes the two-dimensional information of the gas thickness in the beam direction inside the operating electrolyzer.

Energy-dispersive X-ray spectroscopy (EDX) was used to characterize the elemental composition of the observed sample areas. An X-ray diffractometer, a Bruker D8 DISCOVER with Cu TWIST-TUBE X-RAY SOURCE, was used. With this, an electron beam is focused and driven line by line over the surface. The beam electron precipitates from the sample of one of the near-nuclear electrons in an atom. One of the higher-energy electrons reaches this energetically more favorable level, while the energy difference is released as an X-ray quantum. The detector detects the energy of the X-ray quantum, which is characteristic of a chemical element. When scanning the surface with these methods, it is possible to detect the distribution of chemical elements.

3 Results and Discussion

The high resolution of synchrotron radiography allowed the calculation of not only the mean volume of water or gas, but also the capacity to visualize the formation and movement of individual gas bubbles in the PTL.

3.1 Bubble Formation

Figure 2a shows a picture of the cell *operando*. In the middle image area is the CCM, and from both the anode and cathode sides, the PTL can be seen. The PTL range is darker because titanium absorbs more beam intensity than the thin CCM, with a total thickness of about $333 \mu\text{m}$. The cathodic catalyst layer can be identified as a dark structure with a thickness of $56 \mu\text{m}$. According to the pictures, the membrane does not seem to be in contact with the cathode PTL. The polarization curves show, however, that the electrochemical reaction has taken place (see Figure 2c). The processed images also show gas bubble production, confirming the normal functioning of the cell. The length of the contact surface is 10 mm , with the field of view of the camera being only 1.2 mm , hence just over 10% is detected. The gap between the CCM and cathodic flow structure is about $500 \mu\text{m}$ -wide and the contours are not clearly recognizable, which is caused by the fabrication of the PTL, e.g., when cutting the PTL with a water jet. The CCM and PTL make contact outside the field of view of the camera.

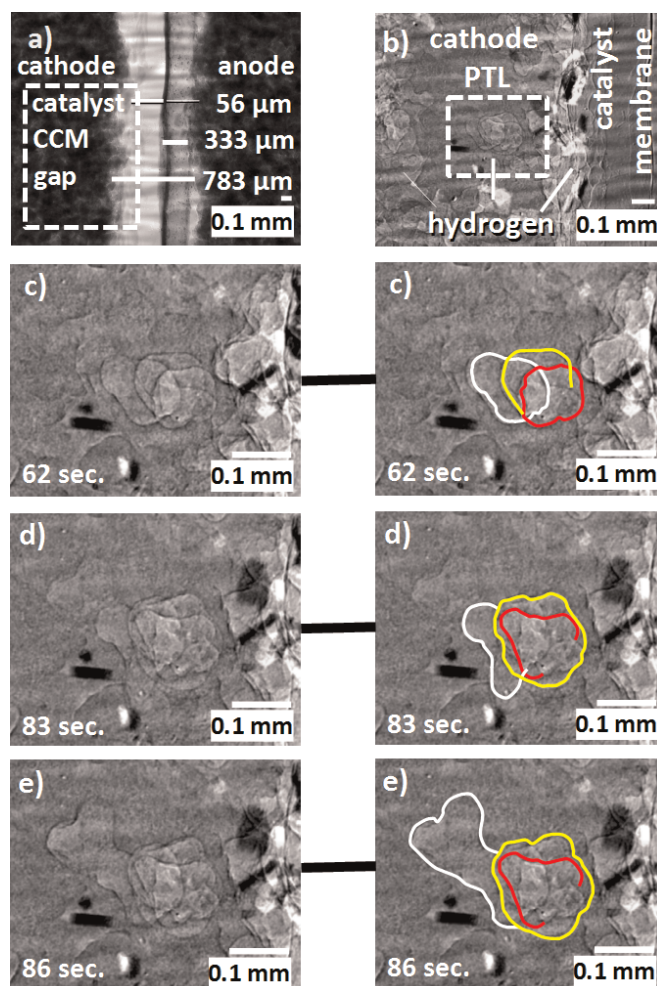


Fig. 2 a) original image; b) cutout cathode, normalized image, only the structures that have changed their position are visible (gas bubbles and catalyst particles); c–e) cutout pore network. The radiograph series shows the growth and propagation of hydrogen bubbles in the pores of the PTL at 0.1 A cm^{-2} .

The synchrotron radiography images show a very good resolution and structures of a few microns can be distinguished.

After image processing, static “objects”, such as the pores of material are filtered out and moving “objects” such as catalyst particles and gas bubbles become visible. The pictures show changes in the cathode PTL during the recording of a polarization curve.

Figures 2c to 2e showing bubble growth and transport in the PTL at a current density of 0.1 A cm^{-2} . A section of the PTL can be seen on the cathode side. This means that gas is produced on the right and transported away to the left with the flow. For a better identification of bubbles, the interesting structures are bordered with colored lines. One also observes elongated, rectangular particles, up to $10 \mu\text{m}$ in length, that absorb much radiation and therefore appear dark. It is the cathode catalyst (platinum).

The image series shows how the bubbles grow and slowly fill the pores so that the shape and configuration of the pores

becomes visible. In the image at 62 s, three bubbles can be seen that fill neighboring pores in the beam direction. Superimposed bubble contours indicate that these effects are not surface effects, but are related to gas transport in the volume.

Pores that became visible through the gas bubbles have diameters of 0.1 to 0.2 mm.

The mercury porosimetry shows a mean pore radius of 6 μm with a lognormal distribution, see Figure 6. Thus, there is a smaller percentage of big pores. There are two reasons why only large pores are visible: First, because Titan PTL is hydrophilic, the bubbles prefer to use large pores for transport; second, because of smaller size, it is difficult to sharply resolve the small pores. Presumably, the small pores which are filled with gas that appears as image noise.

It was also observed that the bubbles consistently use the same pore network, and that bubble movement through the connected pores is repeated in the time interval. Preferred pathways exist for gas transport in the PTL. As the current density increases, more hydrogen bubbles can be seen. The movement of bubbles through the pore network increases in speed. Increasing gas production then opens up new “pore pathways”.

This images shows how the bubble in the PTL structure grows at a certain distance to the catalyst. It is not clear, however, whether this is the effect described by Lubetkin [8] or if the gas is directed from the catalyst layer through a micropore that is not visible at this resolution.

As the bubbles grow, the contours of several connections with neighboring pores simultaneously become visible, thus making alternative pathways for further bubble propagation visible. As can be seen in the image at 86 s, the bubble grows and spreads and then two neighboring pore throats simultaneously become visible. After a few seconds, the bubble spreads into one of the two neighboring pores. The pressure builds up and the bubble expands through the widened-in-its-circumference pore neck. This process is known as “one-throat-at-a-time” [28]. The limiting pore necks have a decisive influence on the gas balance and the pressure gradient in the PTL.

3.2 Degradation of the Anodic Catalyst Layer

During the first test, strong degradation and detachment of the anode catalyst layer was observed. Before the measurement with the synchrotron beam, the cell was wetted with water for 30 minutes. A polarization curve was then recorded. The cell was observed using the synchrotron beam during humidification and operation. However, catalyst removal only became visible with the operation of the cell. This excludes the synchrotron beam as a factor in the catalyst removal.

The current density was increased in steps of 0.1 A cm^{-2} every 10 min up to 0.6 A cm^{-2} . At such low current densities, the cell has already reached a voltage of 2.2 V, and so the current has not been increased further. The polarization plot (see Figure 5) indicates the influence of the water flow rate on the performance. The cell operates stable only at the low flow rate (0.1 mL min^{-1}) the performance drops down a little bit. Figure 3 shows the image series depicting the catalyst degradation.

The CCM, which is contacted on both sides by the PTL, can be seen vertically in the center of the image. At the first operating point with no current, no catalyst degradation was observed (Figure 3a). When the current was switched on, some particles moved within the catalyst layer (Figure 3b). The subsequent images (Figures 3c–e) show, however, more small particles, as well as larger agglomerates with a length of up to 100 μm , detached from the catalyst layer and moved towards the anode side. This degradation process is not dependent on the radiation; otherwise, it would have begun when the measurement started. Rather, this detachment depends on the electrochemical processes and mainly affects the anode catalyst. On the cathode side, a minimal change can be observed in the catalyst layer, but is negligible compared to the anode side. The separated catalyst particles move with the water flow from the CCM to the channel. The type of movement proves that the particles move through the pores of the PTL. The particles tumble to one place, and then move in leaps and bounds. The particles are swirled with the flow into a pore and then carried along to the next one. When assembling the cell, the rubber seal between the PTL and end plate was installed. During pressing, the rubber seal fits into the surface roughness and prevents the formation of a gap. The degradation and detachment process occur within the first hour of operation. After this, no further changes were registered in the catalyst layer. One of the reasons why such severe degradation was observed could be the mechanical stress that the CCM was exposed to when installing in such a non-conventional cell. However, this does not explain why the cathode side is not so heavily affected. Another possible reason for is the decal process that was used in the manufacturing process. A suboptimal adaption of the manufacturing protocol on the geometry of the test cell may be responsible for poor coating adhesion.

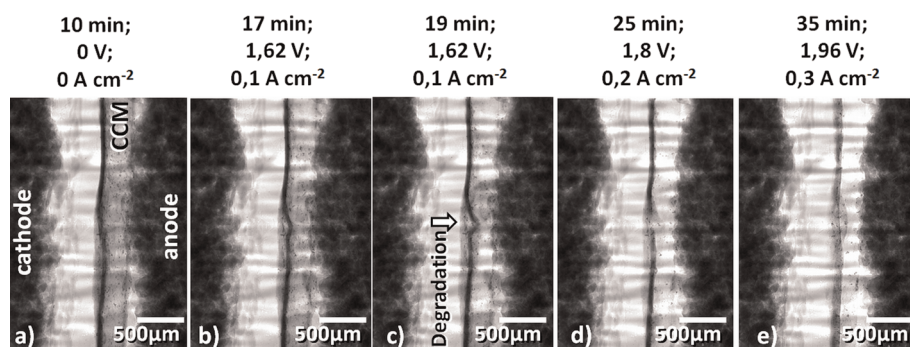


Fig. 3 (a–e) Synchrotron radiographs showing the change and thinning of the catalyst layer.

3.3 EDX

To determine the distribution of chemical elements in the PTL after the test, the PTL was analyzed by means of EDX. Thus, the element distribution on the PTL surface was investigated (Figure 4). To determine the distribution of the elements inside the porous structure, the sintered bodies were subsequently embedded and ground down to the sample center. Then, an EDX analysis of the inner PTL structure was performed. It was only present on the anode in the pristine state and Pt only on the cathode after cell operation EDX showed that Pt and Ir are present on both electrodes, on the surface and inside the PTL structure. The cell was in operation for almost 24 h, which did not explain such strong catalyst degradation. No catalyst inside the membrane was detected, suggesting that the mutual catalyst migration does not pass through the Nafion membrane, but through the imperfections in the seal. The fact that the catalyst particles were also found in the pores of the PTL confirms the movement of the catalyst particles through the pores of the PTL.

4 Conclusions

Synchrotron radiography is a suitable method for visualizing bubble formation and transport in porous structures. The unique and innovative cell design allows for the visualization

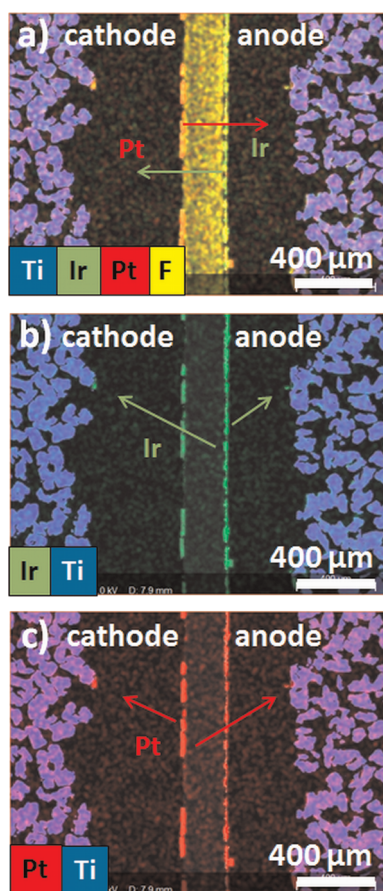


Fig. 4 Post mortem EDX analysis of the titanium HDH sample: a) distribution of chemical elements; b) Ir distribution; c) Pt distribution.

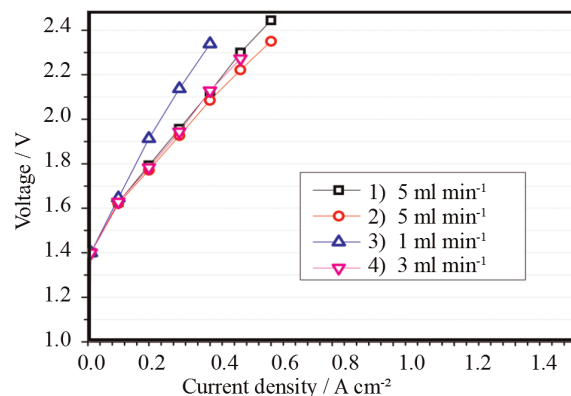


Fig. 5 Polarization plots at ambient temperature and different flow rates.

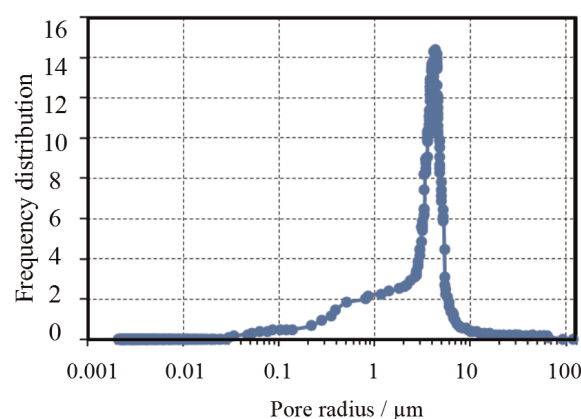


Fig. 6 Pore radius distribution measured with mercury porosity measurements.

of bubble formation and transport in the PTL. In this study, individual bubbles that fill the pores and propagate through the PTL were successfully visualized. The gas flow from the CCM to the channel was also observed. When propagating through the PTL, the bubbles used preferred pathways with low flow resistance. With increasing current density, new transport pathways were activated.

Strong particle detachment from the anode catalyst layer was also observed. During a subsequent in-plane synchrotron measurement, the temporal and operating-point dependence of the catalyst detachment was investigated. Catalyst detachment does not depend on the operating conditions and always takes place after the cell has been put into operation. The mutual diffusion of catalysts was also detected, as were Pt and Ir diffusions through the Nafion membrane after such a short operating time (24 h).

Acknowledgements

The authors would like to thank HZB for granting beam time and numerous technical discussions. Furthermore, financial support within the NeStPEL project, provided by the German Federal Ministry for Economic Affairs and Energy (BMWi, Förderkennzeichen 03ET6044A), is highly appreciated.

References

- [1] A. Roy, S. Watson, D. Infield, *International Journal of Hydrogen Energy* **2006**, *31*, 1964.
- [2] O. F. Selamet, P. Deevanhxay, S. Tsushima, S. Hirai, *ECS Transactions* **2013**, *58*, 353.
- [3] E. Leonard, A. D. Shum, S. Normile, D. C. Sabarirajan, D. G. Yared, X. Xiao, I. V. Zenyuk, *Electrochimica Acta* **2018**, *276*, 424.
- [4] M. A. Hoeh, T. Arlt, I. Manke, J. Banhart, D. L. Fritz, W. Maier, W. Lehnert, *Electrochemistry Communications* **2015**, *55*, 55.
- [5] J. Seweryn, J. Biesdorf, T. J. Schmidt, P. Boillat, *Journal of The Electrochemical Society* **2016**, *163*, F3009.
- [6] H. Markötter, I. Manke, J. Haußmann, T. Arlt, M. Klages, P. Krüger, C. Hartnig, J. Scholta, B. R. Müller, H. Riesemeier, *Micro and Nano Letters* **2012**, *7*, 689.
- [7] T. Arlt, I. Manke, K. Wippermann, C. Tötzke, H. Markötter, H. Riesemeier, J. Mergel, J. Banhart, *Electrochemistry Communications* **2011**, *13*, 826.
- [8] T. Arlt, M. Klages, M. Messerschmidt, H. Riesemeier, J. Scholta, J. Banhart, I. Manke, *ECS Electrochemistry Letters* **2014**, *3*, F7.
- [9] C. Netzeband, T. Arlt, K. Wippermann, W. Lehnert, I. Manke, *Journal of Power Sources* **2016**, *327*, 481.
- [10] J. Hinebaugh, J. Lee, C. Mascarenhas, A. Bazylak, *Electrochimica Acta* **2015**, *184*, 417.
- [11] J. Lee, S. Chevalier, R. Banerjee, P. Antonacci, N. Ge, R. Yip, T. Kotaka, Y. Tabuchi, A. Bazylak, *Electrochimica Acta* **2017**, *236*, 161.
- [12] S. Lubetkin, *Chemical Society Reviews* **1995**, *24*, 243.
- [13] Q. Chen, L. Luo, H. S. White, *Langmuir* **2015**, *31*, 4573.
- [14] S. H. Ahn, I. Choi, H.-Y. Park, S. J. Hwang, S. J. Yoo, E. Cho, H.-J. Kim, D. Henkensmeier, S. W. Nam, S.-K. Kim, *Chemical Communications* **2013**, *49*, 9323.
- [15] G. M. Whitney, C. W. Tobias, *AIChE Journal* **1988**, *34*, 1981.
- [16] S. Burgmann, M. Blank, O. Panchenko, J. Wartmann, *Experiments in Fluids* **2013**, *54*, 1513.
- [17] J. Lee, J. Hinebaugh, A. Bazylak, *Journal of Power Sources* **2013**, *227*, 123.
- [18] R. Borup, J. Meyers, B. Pivovar, Y. S. Kim, R. Mukundan, N. Garland, D. Myers, M. Wilson, F. Garzon, D. Wood, *Chemical Reviews* **2007**, *107*, 3904.
- [19] C. Rakousky, U. Reimer, K. Wippermann, M. Carmo, W. Lueke, D. Stolten, *Journal of Power Sources* **2016**, *326*, 120.
- [20] S. Cherevko, A. A. Topalov, A. R. Zeradjanin, G. P. Keeley, K. J. Mayrhofer, *Electrocatalysis* **2014**, *5*, 235.
- [21] A. Laconti, H. Liu, C. Mittelsteadt, R. McDonald, *ECS Transactions* **2006**, *1*, 199.
- [22] S. Grigoriev, K. Dzhus, D. Bessarabov, P. Millet, *International Journal of Hydrogen Energy* **2014**, *39*, 20440.
- [23] M. Debe, S. Hendricks, G. Vernstrom, M. Meyers, M. Brostrom, M. Stephens, Q. Chan, J. Willey, M. Hamden, C. K. Mittelsteadt, *Journal of the Electrochemical Society* **2012**, *159*, K165.
- [24] Q. Feng, X. Z. Yuan, G. Liu, B. Wei, Z. Zhang, H. Li, H. Wang, *Journal of Power Sources* **2017**, *366*, 33.
- [25] O. Panchenko, E. Borgardt, W. Zwaygardt, F. J. Hackemüller, M. Bram, N. Kardjilov, T. Arlt, I. Manke, M. Müller, D. Stolten, W. Lehnert, *Journal of Power Sources* **2018**, *390*, 108.
- [26] D. S. Hussey, J. M. LaManna, E. Baltic, D. L. Jacobson, *Nuclear Instruments and Methods in Physics Research Section A: Accelerators, Spectrometers, Detectors and Associated Equipment* **2017**, *866*, 9.
- [27] W. Görner, M. Hentschel, B. Müller, H. Riesemeier, M. Krumrey, G. Ulm, W. Diete, U. Klein, R. Frahm, *Nuclear Instruments and Methods in Physics Research Section A: Accelerators, Spectrometers, Detectors and Associated Equipment* **2001**, *467*, 703.
- [28] X. Li, Y. Yortsos, *AIChE Journal* **1995**, *41*, 214.